Chemically active droplets in crowded environments

Jacques D. Fries [1], Roxanne Berthin [1], Chengjie Luo,[2] Marie Jardat [1], David Zwicker [2],
Vincent Dahirel [1], and Pierre Illien [1,*]

[1]*Sorbonne Université, CNRS, Physico-Chimie des Électrolytes et Nanosystèmes Interfaciaux (PHENIX), 4 Place Jussieu, 75005 Paris, France*
[2]*Max Planck Institute for Dynamics and Self-Organization, Am Faßberg 17, 37077 Göttingen, Germany*

Biomolecular condensates are essential for cellular organization and result from phase separation in systems far from thermodynamic equilibrium. Among various models, chemically active droplets play a significant role, and consist of proteins that switch between attractive and repulsive states via nonequilibrium chemical reactions. While field-based simulations have provided insights into their behavior, these coarse-grained approaches fail to capture molecular-scale effects, particularly in crowded cellular environments. Macromolecular crowding, a key feature of intracellular organization, strongly influences molecular transport within condensates, yet its quantitative impact remains underexplored. This study investigates the interplay between chemically active droplets and crowders by using particle-based models, that provide molecular insight, and a field-based model, that complements this picture. Surprisingly, crowding reduces droplet size while expanding the overall dense phase volume, challenging equilibrium-based expectations. This effect arises from the interplay between depletion interactions, diffusion hindrance, and nonequilibrium particle fluxes. Our findings provide a step towards a more comprehensive understanding of chemically active droplets in complex, realistic cellular environments.

I. INTRODUCTION

Biomolecular condensates, which play a key role in the spatial organization of the nucleus, cytoplasm, and membranes of biological cells, have become a central topic in biophysics [1–5]. These microscopic or nanoscopic assemblies of proteins typically result from a local phase separation phenomenon, that occurs in a system maintained very far from thermodynamic equilibrium: this makes their modeling particularly challenging.

Among the different models of biomolecular condensates, chemically active droplets now play an important role [6]. They are assumed to be made of proteins that coexist under two forms: in a form called droplet material, the proteins attract each other through short-range interactions, and in another form, they simply repel each other and do not take part in the formation of droplets. The transitions between these two forms occur via nonequilibrium chemical reactions [7–10]. Such chemically active droplets have been studied through field-based simulations [11–13] and aggregation-fragmentation models [14], where the interactions between the different species is encoded in a free energy functional, and which have recently been extended to more complex descriptions, that account for electrostatic interactions [15], the effect of confinement [16], or the role of enzyme molecules [17].

Nevertheless, this coarse-grained approach cannot predict accurately the structure and dynamics of biomolecular condensates in situations where microscopic details matter the most [18]. For instance, a central aspect of intracellular organization is macromolecular crowding: metabolic processes are known to take place in strongly dense environments [19–23], and biomolecular condensates thus operate under conditions where the transport of droplet material is strongly affected by the presence of crowders [24–26]. Even though the effect of macromolecular crowding on the phase separation of *in vitro* polymers at equilibrium is well known [27], its role in the context of biomolecular condensates has not been studied in minimal physical models yet.

In this article, we study the interplay between chemically active droplets and crowders through two numerical approaches: a particle-based description, where the proteins and crowders are represented explicitly as interacting Brownian particles [28,29], and a field-based description, where the crowders are represented as an additional density field [13]. In both approaches, we study the effect of crowding on the structure and dynamics of active emulsions. In agreement with the behavior of equilibrium systems, the presence of crowders increases the overall volume of the dense phase. This reflects the influence of thermodynamic driving forces, such as depletion interactions. However, this larger volume is surprisingly split into smaller droplets, against the intuition that crowding favors condensation. We show that different crowding-induced mechanisms, such as diffusion hindering or chemical reaction acceleration, contribute to this observation. This work is a first step towards a quantitative description of chemically active droplets in complex environments, going beyond idealized descriptions.

II. PARTICLE-BASED SIMULATIONS

We first simulate a three-dimensional suspension of interacting particles, obeying Brownian (i.e., overdamped

---

*Contact author: pierre.illien@sorbonne-universite.fr

064410-1

Langevin) dynamics, which are integrated with a standard algorithm [30,31] (see Appendix A for details on numerical simulations). The suspension is made of three species, denoted by *A*, *B*, and *C*. The *B* particles interact via an attractive Lennard-Jones potential and are therefore the droplet material [28]. The interaction parameter ε of this potential is chosen in such a way that the *B* particles show liquid-gas coexistence at the considered density and at equilibrium. All the other interactions between particles are repulsive (we use the Weeks-Chandler-Andersen potential [32] to model their interactions).

B particles may convert into *A* particles, and vice versa, and the corresponding conversions occur via two distinct pathways: a passive pathway, in which detailed balance is fulfilled, and an active pathway, in which detailed balance is broken [28]. Let us denote by $\mathcal{C}$ and $\mathcal{C}'$ two configurations which only differ by the species of one particle, and by $k^{\mathrm{p}}_{\mathcal{C},\mathcal{C}'}$ (resp. $k^{\mathrm{a}}_{\mathcal{C},\mathcal{C}'}$) the rate at which the conversion from $\mathcal{C}$ to $\mathcal{C}'$ occurs through the passive (respectively active) pathway. On one hand, the detailed balance conditions impose $k^{\mathrm{p}}_{\mathcal{C}',\mathcal{C}}/k^{\mathrm{p}}_{\mathcal{C},\mathcal{C}'} = \exp\{-\beta[E(\mathcal{C}) - E(\mathcal{C}')]\}$, where $\beta = (k_{\mathrm{B}}T)^{-1}$, and where $E(\mathcal{C})$ is the energy of configuration $\mathcal{C}$. On the other hand, the active reaction rates fulfill $k^{\mathrm{a}}_{\mathcal{C}',\mathcal{C}}/k^{\mathrm{a}}_{\mathcal{C},\mathcal{C}'} = \exp\{-\beta[E(\mathcal{C}) - E(\mathcal{C}') + \kappa_{\mathcal{C}',\mathcal{C}}\Delta\mu]\}$ where $\Delta\mu$ is a chemical drive fixed to $8k_{\mathrm{B}}T$ unless specified otherwise, and $\kappa_{\mathcal{C}',\mathcal{C}} = 1$ if the transition from $\mathcal{C}'$ to $\mathcal{C}$ implies the formation of a *B* particles and -1 otherwise. The prefactors that remain to be determined are chosen in such a way that passive (respectively active) reactions dominate in the dilute (respectively dense) phase [28]. Finally, the particles of species *C* do not take part in the reactions, and play the role of crowders. While the volume fractions of *A* and *B* are fixed ($\phi_A + \phi_B = 0.025$), the volume fraction of the crowders is tuned in such a way that the total volume fraction $\phi = \phi_A + \phi_B + \phi_C$ varies from 0.05 to 0.425.

We previously showed that, in these simulations, the interplay between pair interactions and nonequilibrium reactions (tuned by the chemical drive $\Delta\mu$) leads to the formation of stable active droplets, which are continuously fed from the outside and destroyed from the inside. Within the framework of active emulsions [6,13], the droplets are "externally maintained." In order to study the effect of crowding on the structure of the resulting active emulsion, the evolution of the system is simulated until it reaches a nonequilibrium steady state. We then compute the volume distribution of the droplets, for different values of the overall volume fraction ϕ [Fig. 1(a)]. Strikingly, we observe that the corresponding average droplet volume [shown in Fig. 1(b)] is a decreasing function of the volume fraction ϕ. This is also verified for other chemical drives ($\Delta\mu = 9k_{\mathrm{B}}T$ or $\Delta\mu = 10k_{\mathrm{B}}T$). In order to check whether this diminution of the droplet volume is associated with an overall shrinking of the dense phase, we also plot on Fig. 1(c) the average volume fraction of the dense phase $\langle\xi\rangle$, defined as the total volume occupied by droplets divided by the volume of the simulation box. We see that $\langle\xi\rangle$ increases with crowding, indicating that, although the volume of the droplets decreases, they must be more numerous. This is confirmed by the plot on Fig. 1(d), that shows the distribution of the number of droplets for different densities of crowders at $\Delta\mu = 8k_{\mathrm{B}}T$.
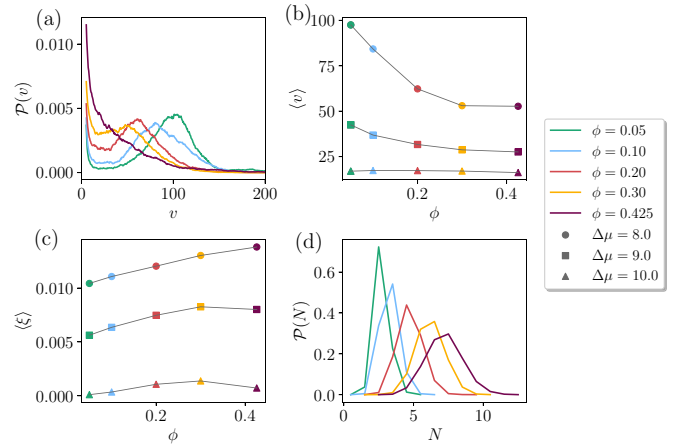

FIG. 1. (a) Probability distribution of the droplet volume in the stationary state, for various values of the total volume fraction ϕ. (b) Average volume of a droplet $\langle v \rangle$ as a function of the total volume fraction ϕ for various chemical drives. Note that for $\Delta\mu = 10k_{\mathrm{B}}T$, the average droplet size is close to the nucleation threshold. (c) Average volume fraction of the dense phase $\langle\xi\rangle$ as a function of the total volume fraction ϕ for various chemical drives. (d) Probability distribution of the number of droplets in the simulation box for various values of the total volume fraction ϕ.

These observations can be compared with what is typically observed at equilibrium, in the absence of reactions. We show in Appendix B that, in the absence of any reactions, the critical interaction energy ε above which the *B* particles form a single cluster decreases with the overall density ϕ. In addition, increasing crowding encourages the condensation of larger and larger droplets [27]. In other words, the average volume fraction of the dense phase $\langle\xi\rangle$ increases with crowding both at equilibrium and out of equilibrium. However, the difference between the two situations resides in the fact that the dense phase is spatially organized differently: at equilibrium the dense phase always forms a single droplet, as opposed to the present nonequilibrium case, where several droplets coexist, and where increased crowding leads to a larger number of smaller droplets.

We now aim at understanding the mechanisms that govern these nonequilibrium effects. Naively, one would expect that increasing the density of crowders has the following consequences: (i) the attraction between the *B* particles should be stronger, because of the depletion induced by the crowders [33–37] (note that we will use the term "depletion" even though *A*, *B* and *C* have the same size); (ii) the mobility of the particles is expected to be smaller when ϕ increases [38–40]. Note that, in an equilibrium situation (i.e., without reactions, or with $\Delta\mu = 0$), since the stationary state is independent of the dynamics, only the effect of depletion actually matters. In what follows, we study separately these effects, in order to understand how they affect the size and number of chemically active droplets that coexist at stationary state.

We start by investigating the effect of crowding on the mobility of the particles, and therefore on the diffusive fluxes that continuously feed and destroy the droplets. To this end, we perform simulations where the crowders are not represented explicitly, but are accounted for implicitly, through
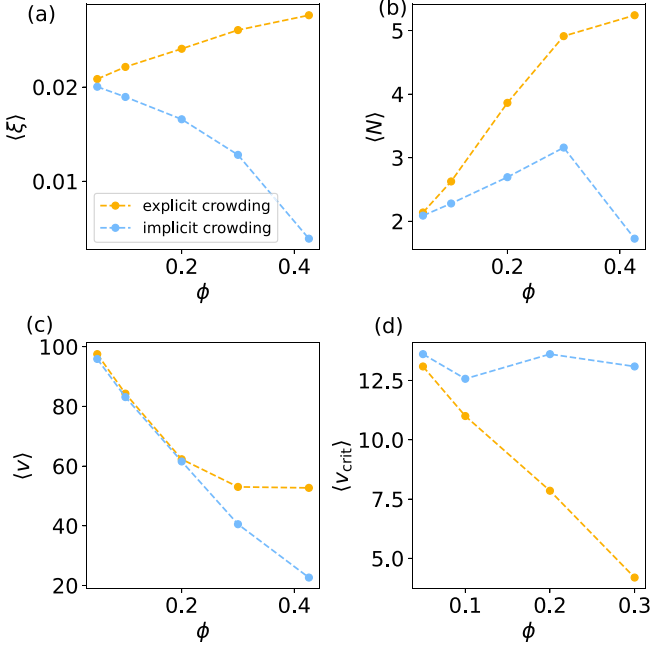
FIG. 2. (a) Average volume fraction of the dense phase $\langle \xi \rangle$, defined as the total volume occupied by droplets divided by the volume of the simulation box, (b) average number of droplets $\langle N \rangle$, (c) average volume of the droplets $\langle v \rangle$, and (d) average critical nucleation volume of the droplets $\langle v_{\mathrm{crit}} \rangle$, as a function of the overall volume fraction ϕ, both in simulations where the crowders are represented explicitly (orange symbols) and implicitly (blue symbols). The chemical drive is $\Delta \mu = 8 k_{\mathrm{B}} T$.

the bare diffusion coefficients of the A and B particles, that become functions of the volume fraction of crowders ϕ_C. The diffusion coefficient for hard spheres in a three-dimensional system can be approximated as $D(\phi_C) \simeq D_0(1 - 2\phi_C)$ [note that this actually exact up to order $O(\phi_C^2)$ [41–43]], where D_0 is the diffusion coefficient of the particles in an infinitely dilute solution. This is the choice we make for the diffusion coefficients of A and B particles in these simulations, which will be called "implicit," as opposed to the previous ones, that will be called "explicit." Importantly, the implicit simulations account for the fact that the diffusion coefficient of the particles decreases with crowding (see Appendix C for a discussion on this aspect), but not for the fact that their interactions are effectively more attractive due to depletion interactions, which allows to decouple the two effects.

In this set of simulations, we measure the average volume fraction of the dense phase $\langle \xi \rangle$, the average number of droplets $\langle N \rangle$, and their average volume $\langle v \rangle$. These observables are shown respectively on Figs. 2(a), 2(b), and 2(c), as a function of the total volume fraction ϕ. We observe that, in the implicit simulations, the average volume fraction of the dense phase $\langle \xi \rangle$ decreases [Fig. 2(a)], whereas the number of droplets increases to a much lesser extent, up to the point where they become unstable [Fig. 2(b)]: this means that the average volume of the droplets decreases, as seen on Fig. 2(c). Therefore, although the implicit simulations correctly predict the diminution of the droplet size with increasing crowding,

they do not account for the fact that the volume of the dense phase increases.

Finally, we also plot the critical nucleation volume as a function of the total volume fraction, for both implicit and explicit simulations [see Fig. 2(d), where $\langle v_{\mathrm{crit}} \rangle$ is measured from the phase portraits of the droplet volume [28], which are shown in Appendix D]. In implicit simulations, the nucleation volume is essentially independent of the total volume fraction. On the contrary, it strongly decreases with crowding in explicit simulations. In other words, in explicit simulations, small droplets are more likely to be stable against fluctuations, and it is therefore easier and easier to nucleate droplets as crowding increases: hence, there are more droplets in explicit simulations than in implicit ones.

In summary, by comparing the two sets of particle-based simulations, we conclude that implicit simulations cannot account for the following observations from the explicit simulations: (i) crowding increases the total volume of the dense phase; and (ii) crowding reduces the critical nucleation volume. Both effects are then related to either the effect of depletion, or to the way active reactions, that are typically density dependent, are implemented.

III. FIELD-BASED SIMULATIONS

To get further insight into the roles of depletion and active reactions, we also perform field-based simulations of active emulsions, in the spirit of Refs. [10,13,44]. In these simulations, the system comprises the three species A, B, and C, just like in particle-based simulations, and a fourth species S, which plays the role of solvent. The state of the system is then described by four density fields $\phi_i(\mathbf{r}, t)$, which obey $\sum_{i\in\{A,B,C,S\}} \phi_i(\mathbf{r}, t) = 1$, so we do not need to describe ϕ_S explicitly. The fields for A, B, C obey the reaction-diffusion equations $\partial_t \phi_i = \nabla \cdot (\lambda_i \phi_i \nabla \mu_i) + R_i$, where λ_i denotes the diffusivity of species i and the net reaction fluxes R_i are

$$R_B = -R_A = 2k_p(1 - \phi_A - \phi_B)\sinh\left(\frac{\beta}{2}(\mu_A - \mu_B)\right)$$
$$+ 2k_a(\phi_A + \phi_B)\sinh\left(\frac{\beta}{2}(\mu_A - \mu_B - \Delta\mu)\right), \quad (1)$$

whereas $R_C = 0$. The two lines in Eq. (1), respectively, describe passive and active contributions with rates k_p and k_a, consistent with the particle-based setup. We show in Appendix E that the results that follow are robust to changes of the functional dependence of the prefactors to the sinh functions, provided that the passive (respectively active) reaction dominate in the dilute (respectively dense) phase. Chemical reactions are driven by the exchange chemical potentials $\mu_i = v\beta\delta F/\delta\phi_i$ following from free energy functional F. For simplicity, we consider a Flory-Huggins free energy

$$F = \frac{k_{\mathrm{B}}T}{v}\int \left[w_B\phi_B + \sum_{i,j\in\{A,B,C,S\}}\chi_{ij}\phi_i\phi_j \right.$$
$$\left. + \sum_{i\in\{A,B,C,S\}}\phi_i\ln\phi_i + \frac{\kappa^2}{2}|\nabla\phi_B|^2 \right]d\mathbf{r}, \quad (2)$$

where the integral is over the entire system and v denotes the molecular volume, which is the same for all species. The first two terms in the square brackets describe the physical interactions among the species, the third term captures translational entropies of all four species, and the last term limits the width of interfaces between coexisting phases to roughly κ in strongly interacting systems. The interaction parameters χ_{ij} are defined as $\chi_{ij} = e_{ij} - (e_{ii} + e_{jj})/2$, where e_{ij} characterizes the interaction strength between species i and j. Specifically, we set $e_{BB} = E_{att} = -5k_BT$ to model the attractive interaction between B particles, and $e_{ij} = E_{rep} = k_BT$ for all other pairs with $i, j \in \{A, B, C\}$, placing the system in a regime where macrophase separation occurs at equilibrium in the absence of reactions. We set the internal energy of species B to $w_B = -4k_BT$ to favor the passive conversion of A to B. Conversely, the active reaction in Eq. (1) is driven by a chemical potential difference $\Delta\mu = 4k_BT$, which drives the conversion of B to A. We simulate these equations in only one dimension since size control of chemically active droplets is similar in all dimensions [44].

We first analyze the typical droplet size emerging from the field-based simulations by measuring the period l of the solutions shown in Appendix E. Figure 3(a) shows that l typically decreases with increasing crowder density ϕ_C, for all tested mobilities λ of the species A,B, and C. While this trend is consistent with the particle-based simulations, crowders in principle also slow down the A and B molecules. To capture this effect, we added the pink solid line to Fig. 3(a), which captures the typical dependency of λ on ϕ_C. The period length along this line [pink curve in Fig. 3(b)] shows a similar trend to the droplet size shown in Fig. 2(c), indicating that crowding generally decrease the size of chemically active droplets.

Our field-theoretic simulations allow disentangling the effect of depletion from the slowdown due to crowding. Figure 3(b) shows that the period l and the average droplet size $\langle v \rangle$ decrease with increasing ϕ_C for fixed mobility λ, so we change the depletion effect without affecting the diffusive kinetics. Concomitantly, the droplet number (green line) and the mean fraction $\langle \xi \rangle$ of the system taken up by the dense phase increase, consistent with the explicit crowding simulations shown in Fig. 2. Moreover, Fig. 3(c) shows that droplets get denser while the dilute phase thins out, indicating that phase separation becomes stronger with increasing ϕ_C. We hypothesize that these compositional changes strongly affect the reaction fluxes R_i given by Eq. (1), possibly explaining the effect on droplet size. Indeed, Fig. 3(d) shows that $|R_B|$ increase with larger ϕ_C, indicating that droplet material B is destroyed more quickly inside the droplets, while its creation in the dilute phase is also accelerated.

IV. DISCUSSION

A simple analytical argument can be invoked to rationalize some of our findings. The classical Lifshitz-Slyozov-Wagner theory of Ostwald ripening can be modified to account for active reactions [7]. Within this framework, in the limit where droplets are sufficiently large to neglect surface tension effects, the typical radius $\mathcal{R}(t)$ of an isolated droplet evolves as (up to numerical prefactors) $\frac{d\mathcal{R}}{dt} = \frac{\mathcal{D}_B\phi_B^0}{\mathcal{R}} - \mathcal{K}_{BA}\mathcal{R}$, where $\mathcal{D}_B$
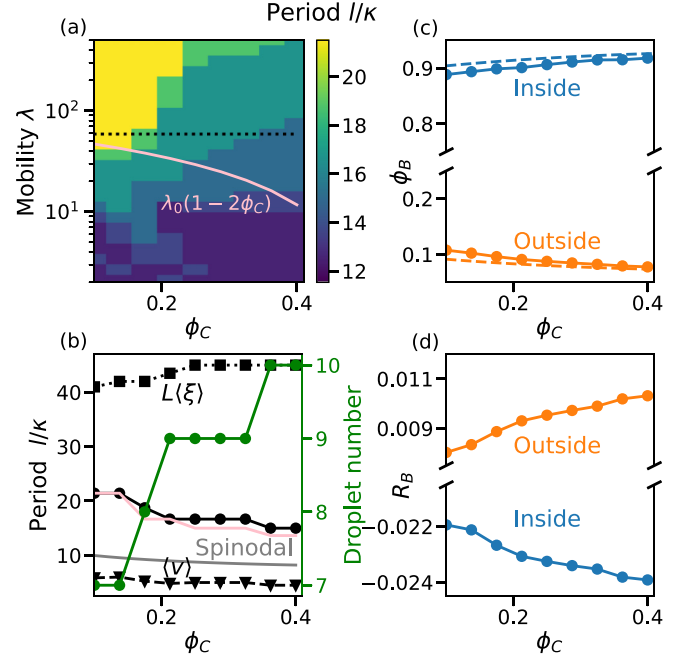

FIG. 3. (a) Pattern period l as a function of the crowder density ϕ_C and the mobility λ of all species. The functional form $\lambda(\phi_C)$ used in the implicit particle-based simulations is shown as the pink solid line. (b) Pattern period l (black disks), mean droplet volume $\langle v \rangle$ (triangles), mean fraction of the system taken up by the dense phase $\langle \xi \rangle$ (squares), and droplet number L/l (green disks) as a function of ϕ_C for fixed mobility $\lambda = \lambda_0 = 58.6$ [corresponding to the black dotted line in (a)]. The pattern period l corresponding to the mobility $\lambda_0(1 - 2\phi_C)$ is shown in pink, aligning with the pink curve in (a), whereas the gray line represents the most unstable length scale predicted from linear stability analysis. (c) Minimal and maximal values of ϕ_B as a function of ϕ_C, corresponding to typical fractions outside and inside droplets, respectively. The dashed curves indicate the values obtained from equilibrium-state calculations in the absence of reactions. (d) Net reaction flux R_B inside (blue) and outside (orange) of droplets as a function of ϕ_C. (a)–(d) Additional parameters are $w_B = -4k_BT$, $\phi_A + \phi_B = 0.4$, $k_a = k_p = 0.01$, $\Delta\mu = 4k_BT$, and linear system size $L = 150\,\kappa$.

is the typical diffusivity of B particles, ϕ_B^0 the typical density of B particles in the dilute phase, and $\mathcal{K}_{BA}$ is the typical rate at which the $B \to A$ reactions take place in the droplets. One finds that the typical droplet size in the stationary state can be estimated as $R \sim \sqrt{\mathcal{D}_B\phi_B^0/\mathcal{K}_{BA}}$. This simple scaling analysis shows how the main consequences of increased crowding (the reduction of the typical diffusivity $\mathcal{D}_B$, the diminution of the typical density in the dilute phase ϕ_B^0, and the enhancement of the reaction rates $\mathcal{K}_{BA}$) all result in an effective reduction of droplet size.

Our particle-based and field-based simulations take this simple analysis much further, by accounting finely for the effect of depletion interactions and for presence of multiple droplets. The three sets of numerical simulations presented in the paper (particle-based simulations with both explicit and implicit crowders on one hand, and field-based simulations on the other hand) allowed us to identify the role played by crowding on the structure of active emulsions, together with
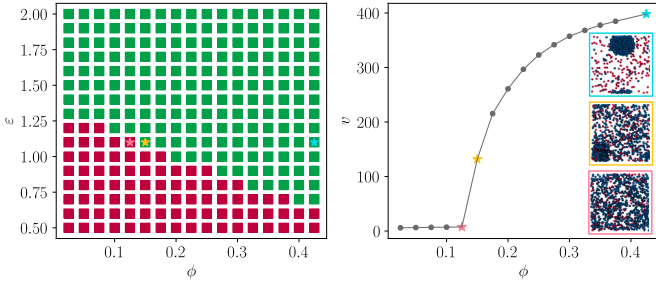
FIG. 4. Left: Phase diagram for the equilibrium simulations: green squares mean that phase separation is observed in the stationary state, whereas red squares mean that no phase separation is observed. Right: Volume of the single droplet observed in the stationary state, as a function of the overall volume fraction ϕ for a fixed value of $\varepsilon = 1.1$. The pink, yellow, and blue stars correspond to three different situations [see left panel for the (ε, ϕ) combination]. Insets are snapshots of these three different simulations.

the underlying mechanisms. We generally observe that, when the volume fraction of crowders increases, the total volume occupied by droplets increases, but that the emulsion is composed of a larger number of smaller droplets. We showed that the reduction of the diffusive fluxes that results from crowding cannot be the only responsible for these observations, as it does not account for neither the overall increase of the volume of the dense phase, nor the facilitated nucleation of droplets. These two effects essentially originate from the depletion interactions induced by the presence of crowders, as confirmed by field-based simulations.
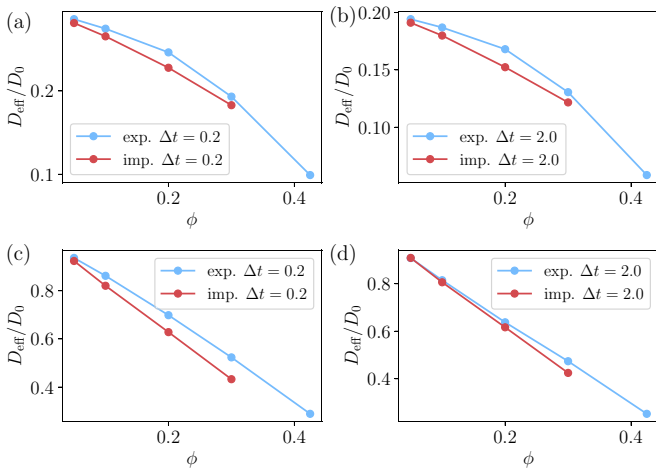
FIG. 5. Diffusion coefficients measured in explicit and implicit particle-based simulations, inside and outside the droplet (top and bottom plots, respectively) and for two time intervals ($\Delta t = 0.2$ on the left, $\Delta t = 2.0$ on the right). The point at $\phi = 0.4$ in implicit simulation is not represented as it corresponds to a system with unstable droplets [see Fig. 6(a)].
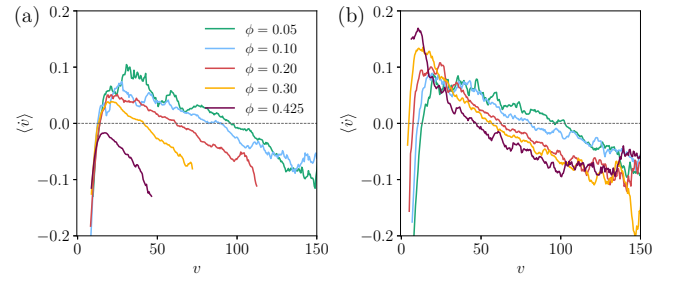

FIG. 6. Phase portrait of the droplet volume, for different values of the total volume fraction, both from implicit (a) and explicit (b) particle-based simulations. The chemical drive is $\Delta\mu = 8k_B T$.

APPENDIX A: PARTICLE-BASED SIMULATIONS

The particle-based simulations were carried out using the LAMMPS computational package [31]. To perform overdamped Langevin dynamics, we start from the evolution equations for the positions of the particles, which read as

$$\frac{d\boldsymbol{r}_n}{dt} = -\frac{D_0}{k_B T} \sum_{m \neq n} \nabla U_{S_n, S_m}(|\boldsymbol{r}_n - \boldsymbol{r}_m|) + \sqrt{2D_0}\,\boldsymbol{\eta}_n(t), \quad \text{(A1)}$$

where D_0 is the bare diffusion coefficient of the particles, $S_n \in \{A, B, C\}$ is the type of particle n, and $\boldsymbol{\eta}_n(t)$ a Gaussian white noise, of zero average, and of variance $\langle \eta_{n,i}(t)\eta_{m,j}(t') \rangle =$
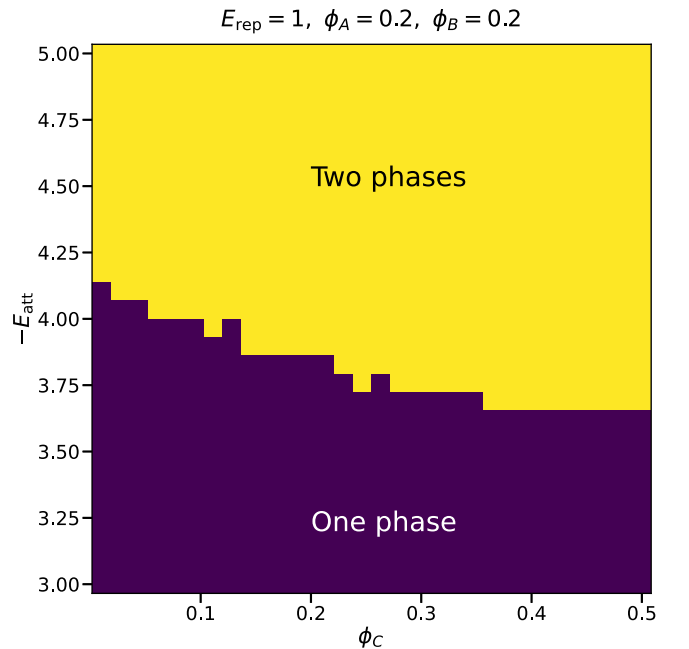

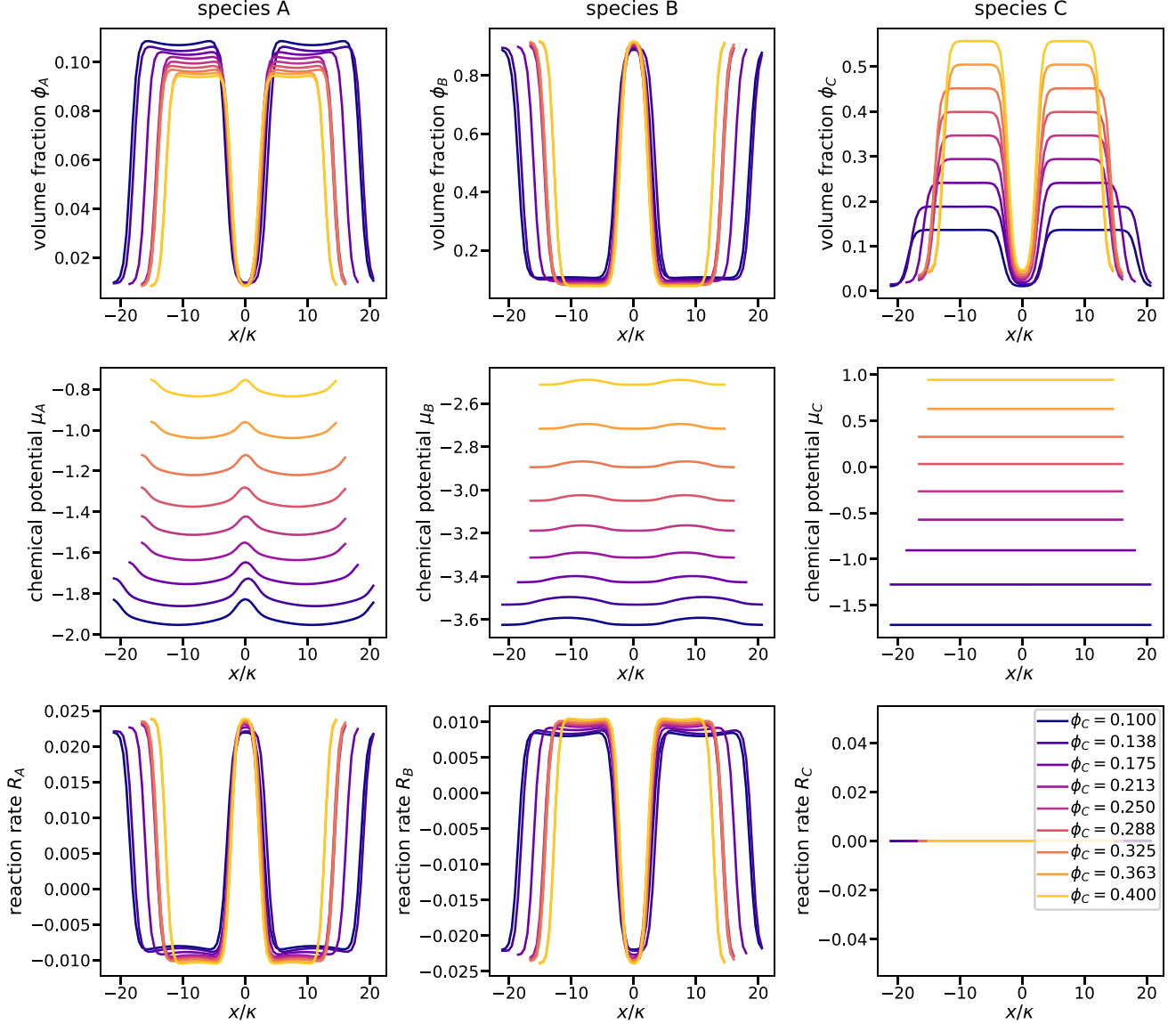FIG. 7. Phase diagram for mean field theory in the absence of reactions.

FIG. 8. Profiles of volume fractions (first row), chemical potentials (second row), and total reaction rates (last row). The parameters are the same as in Fig. 3 in the main text, and the reaction rates are the ones given in Eq. (1) of the main text. For clarity, we plot two periods and shift the center of droplets to $x = 0$.

$\delta_{ij}\delta(t - t')$. Depending on the species of the particles, the potential U_{S_n, S_m} is either a truncated and shifted Lennard-Jones potential

$$U_{B,B}(r) = [U_\varepsilon(r) - U_\varepsilon(r_c)]\theta(r_c - r), \quad (A2)$$

where

$$U_\varepsilon(r) = 4\varepsilon\left[\left(\frac{\sigma}{r}\right)^{12} - \left(\frac{\sigma}{r}\right)^6\right] \quad (A3)$$

and where the cutoff length is $r_c = 2.5\sigma$, or a Weeks-Chandler-Andersen potential

$$U_{A,\{A,B,C\}}(r) = U_{C,\{A,B,C\}}(r) = [U_{\varepsilon'}(r) + \varepsilon']\theta(2^{1/6}\sigma - r). \quad (A4)$$

The energy parameters are $\varepsilon = 2k_BT$ and $\varepsilon' = k_BT$.

We use the command "fix Brownian" of the LAMMPS package, that integrates the evolution equations of the positions of particles thanks to a forward Euler-Maruyama scheme [30]:

$$\boldsymbol{r}_n(t + \delta t) = \boldsymbol{r}_n(t) + \sqrt{2D_0\delta t}\boldsymbol{\zeta} - \delta t \frac{D_0}{k_BT}\sum_{m \neq n}\boldsymbol{\nabla}U_{S_n, S_m}(r_{mn}), \quad (A5)$$

where $\delta t = 2 \times 10^{-4}$ and $\boldsymbol{\zeta}$ is a random vector drawn from a normal distribution of mean 0 and unit variance. These simulations were performed using a cubic box of length 27.144 with periodic boundary conditions. The initial number of each species is $N_A^0 = 200$, $N_B^0 = 800$, and $N_C^0 \in \{0, 900, 2820, 6640, 10460, 15280\}$. In the initial

configurations, the particles are initially located on a face-centered-cubic lattice. The initial configurations are equilibrated for 10^5 time steps. For each set of parameters, we carried out 10 different runs with different initial conditions, and different seeds in the Brownian dynamics command "fix Brownian."

APPENDIX B: EFFECT OF CROWDING AT EQUILIBRIUM

We see that the critical value of ε above which phase separation is observed decreases with the overall volume fraction. Furthermore, the average droplet volume, which also corresponds to the volume of the dense phase at equilibrium (since there is only one droplet) is an increasing function of ϕ (Fig. 4, right panel). This means that crowding facilitates the phase separation in this equilibrium system. This is consistent with the expectation that crowders increase the effective attraction between B particles because of depletion effects.

Concerning the impact of crowding on the mobility of the particles, we do not expect it to play any role in an equilibrium system. Indeed, at equilibrium, any change in the dynamics of the particles will not affect the stationary state, but only the time at which this state is reached from a nonequilibrated initial condition. For example, the phase diagram shown on Fig. 4 is independent of the diffusion coefficients of the particles. On the contrary, for a nonequilibrium system, the steady state can be strongly influenced by the dynamics, and this is what we investigate in the main text.

APPENDIX C: DIFFUSION COEFFICIENT IN IMPLICIT AND EXPLICIT PARTICLE-BASED SIMULATIONS

In the simulations with "implicit crowding" that are described in Sec. II, the crowders C are removed, and the diffusion coefficient of A and B particles is modified to account for crowding. It is assumed to depend on ϕ_C as $D(\phi_C) = D_0(1 - 2\phi_C)$. In order to show that the implicit simulations correctly account for crowding-induced diffusion hindrance, we measure the effective diffusion coefficient of A and B particles as a function of ϕ in both explicit and implicit simulations, in the dense phase and in the dilute phase. The effective diffusion coefficient is estimated as $D_{\mathrm{eff}} = \langle[\mathbf{r}_i(t + \Delta t) - \mathbf{r}_i(t)]^2\rangle/(6\Delta t)$ where the average runs over all particles that belong either to the dense or dilute phase, and over multiple realizations.

We verify that the particles A and B have the same effective diffusivity, both in the dilute and dense phases, in implicit and explicit crowding simulations. The results are depicted in Fig. 5 for two time intervals ($\Delta t = 0.2$ or 2.0). For reference, we recall that the unit time in our simulations corresponds to the time necessary to diffuse over a distance equal to the radius of a particle.

APPENDIX D: PHASE PORTRAITS FROM EXPLICIT SIMULATIONS

We show on Fig. 6 the phase portrait associated with the dynamics of the droplets, i.e., the typical derivative of the volume as a function of the volume. This curve typically crosses the horizontal axis twice, therefore defining two fixed points:
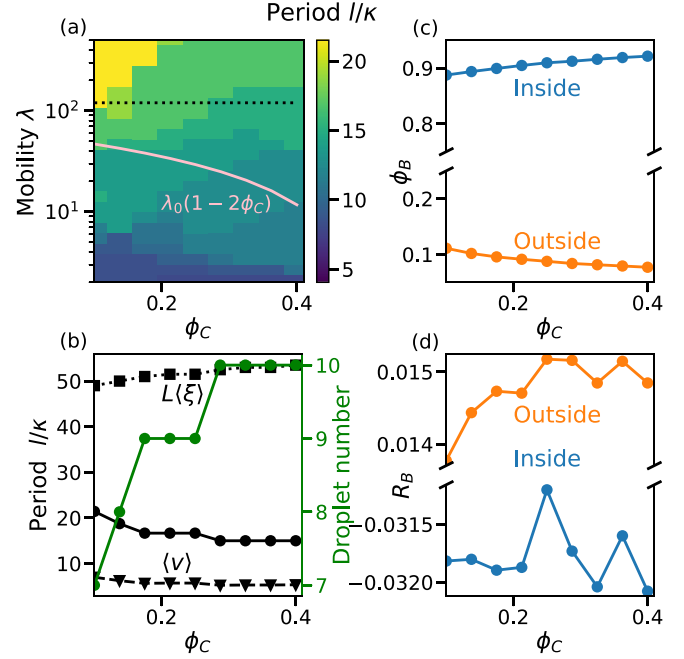

FIG. 9. (a) The pattern period in the field-based simulation using reaction (E2), shown as a color gradient, as a function of the density of crowders ϕ_C and of the mobility λ of species A, B, and C, which are assumed to be equal and which are tuned independently of ϕ_C. The pink solid line shows the typical dependency of the mobility over ϕ_C as implemented in the implicit particle-based simulations. (b) For a fixed mobility $\lambda = \lambda_0 = 58.6$ [indicated by the black dotted line in (a)], the pattern period and the number of droplets are plotted as functions of the crowder density ϕ_C in black and green, respectively. (c) The maximum value of ϕ_B inside droplets at the droplet center x_1 and the minimum value of ϕ_B outside droplets at the midpoint between two droplets x_2. (d) The net reaction rate R_B at x_1 and x_2 in orange and blue, respectively. Additional parameters are $w_B = -4$, $\phi_A + \phi_B = 0.4$, $k_a = k_p = 0.01$, $\Delta\mu = 4$, and $\kappa = 1$.

a stable one, that corresponds to the stable droplet radius that results from interrupted Ostwald ripening, and an unstable one, that is the critical nucleation volume v_{crit} [28], which is plotted as a function of ϕ, both for explicit and implicit simulations, in the main text [Fig. 2(d)].

APPENDIX E: FIELD-BASED SIMULATIONS

Before examining the effects of crowding on active reactions, we first focus on the equilibrium system without reactions. To identify the equilibrium states, we minimize the total free energy using a recently developed package [46], which determines whether the system forms a single phase or undergoes phase separation for a given set of parameters. To find conditions that reproduce behavior similar to particle-based simulations, we vary the interaction strength E_{att} and the crowder volume fraction ϕ_C. The resulting equilibrium phase diagram, shown in Fig. 7, reveals that a weaker attraction (lower $-E_{\mathrm{att}}$) is required to induce phase separation as ϕ_C increases. This trend is qualitatively consistent with the particle-based simulations results shown in Fig. 4.
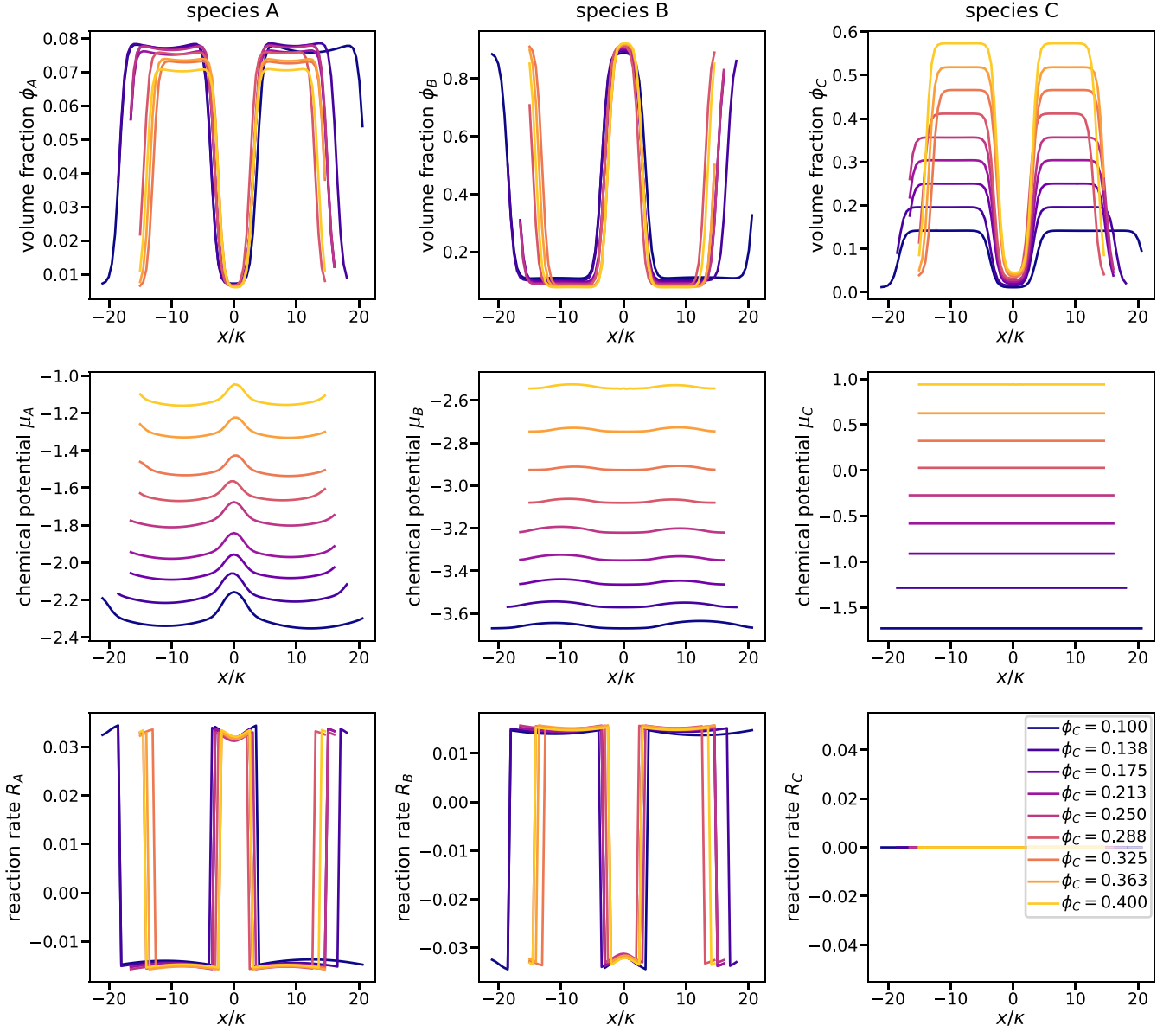
FIG. 10. Profiles of volume fractions (first row), chemical potentials (second row), and total reaction rates (last row) using reaction rates given by Eq. (E2). The parameters are the same as in Fig. S3. For clarity, we plot two periods and shift the center of droplets to $x = 0$.

We perform numerical simulations of the reaction-diffusion equation

$$\partial_t \phi_i = \nabla \cdot (\lambda_i \phi \nabla \mu_i) + R_i \qquad (E1)$$

on an equidistantly discretized grid, using second-order finite differences to approximate differential operators [47]. The chemical potential gradients $\nabla \mu_i$ are evaluated on a staggered grid to ensure material conservation. Time integration is carried out using an explicit Euler scheme. The simulation domain has a size $L = 150\kappa$ with 300 grid points, and the system is evolved up to $t = 100\,000$. We define $\langle \xi \rangle$ as the total area where $\phi_B > (\phi_B^{\max} + \phi_B^{\min})/2$, which we interpret as the interior of the droplets. Here, $\phi_B^{\max}$ and $\phi_B^{\min}$ denote the maximum and minimum values of ϕ_B, respectively.

Figure 8 shows the final profiles over two pattern periods, including volume fractions, chemical potentials, and reaction rates for various values of ϕ_C.

For completeness, we also replace the reaction by

$$R_B = -R_A = 2k_p \, \theta\left(\frac{1}{2} - \phi_B\right) \sinh\left(\frac{\beta}{2}(\mu_A - \mu_B)/2\right)$$
$$+ 2k_a \, \theta\left(\phi_B - \frac{1}{2}\right) \sinh\left(\frac{\beta}{2}(\mu_A - \mu_B - \Delta\mu)\right), \quad (E2)$$

where $\theta(x)$ is the Heaviside function, and show the effects of crowders in Fig. 9 (see also Fig. 10 for the associated profiles of volume fractions, chemical potentials, and reaction rates). The overall trend is consistent with Fig. 2 in the main text, suggesting that the model is robust to changes of the precise functional form of the prefactors of the sinh functions.

[1] A. A. Hyman, C. A. Weber, and F. Jülicher, Liquid-liquid phase separation in biology, Annu. Rev. Cell Dev. Biol. **30**, 39 (2014).

[2] B. Gouveia, Y. Kim, J. W. Shaevitz, S. Petry, H. A. Stone, and C. P. Brangwynne, Capillary forces generated by biomolecular condensates, Nature (London) **609**, 255 (2022).

[3] Y. Shin and C. P. Brangwynne, Liquid phase condensation in cell physiology and disease, Science **357**, eaaf4382 (2017).

[4] S. Alberti and D. Dormann, Liquid–liquid phase separation in disease, Annu. Rev. Genet. **53**, 171 (2019).

[5] S. Alberti, A. Gladfelter, and T. Mittag, Considerations and challenges in studying liquid-liquid phase separation and biomolecular condensates, Cell **176**, 419 (2019).

[6] C. A. Weber, D. Zwicker, F. Jülicher, and C. F. Lee, Physics of active emulsions, Rep. Prog. Phys. **82**, 064601 (2019).

[7] D. Zwicker, A. A. Hyman, and F. Jülicher, Suppression of Ostwald ripening in active emulsions, Phys. Rev. E **92**, 012317 (2015).

[8] D. Zwicker, R. Seyboldt, C. A. Weber, A. A. Hyman, and F. Julicher, Growth and division of active droplets provide a model for protocells, Nat. Phys. **13**, 408 (2017).

[9] J. D. Wurtz and C. F. Lee, Chemical-reaction-controlled phase separated drops: Formation, size selection, and coarsening, Phys. Rev. Lett. **120**, 078102 (2018).

[10] J. Kirschbaum and D. Zwicker, Controlling biomolecular condensates via chemical reactions, J. R. Soc. Interface **18**, 20210255 (2021).

[11] S. C. Glotzer, D. Stauffer, and N. Jan, Monte Carlo simulations of phase separation in chemically reactive binary mixtures, Phys. Rev. Lett. **72**, 4109 (1994).

[12] J. J. Christensen, K. Elder, and H. C. Fogedby, Phase segregation dynamics of a chemically reactive binary mixture, Phys. Rev. E **54**, R2212 (1996).

[13] D. Zwicker, The intertwined physics of active chemical reactions and phase separation, Curr. Opin. Colloid Interface Sci. **61**, 101606 (2022).

[14] M. S. Turner, P. Sens, and N. D. Socci, Nonequilibrium raft-like membrane domains under continuous recycling, Phys. Rev. Lett. **95**, 168301 (2005).

[15] C. Luo, N. Hess, D. Aierken, Y. Qiang, J. A. Joseph, and D. Zwicker, Condensate size control by net charge, ACS Macro Lett. **14**, 1484 (2025).

[16] R. Rossetto, G. Wellecke, and D. Zwicker, Binding and dimerization control phase separation in a compartment, Phys. Rev. Res. **7**, 023145 (2025).

[17] M. W. Cotton, R. Golestanian, and J. Agudo-Canalejo, Catalysis-induced phase separation and autoregulation of enzymatic activity, Phys. Rev. Lett. **129**, 158101 (2022).

[18] G. L. Dignon, R. B. Best, and J. Mittal, Biomolecular phase separation: From molecular driving forces to macroscopic properties, Annu. Rev. Genet. **71**, 53 (2020).

[19] S. B. Zimmerman and A. P. Minton, Macromolecular crowding: Biochemical, biophysical, and physiological consequences, Annu. Rev. Biophys. Biomol. Struct. **22**, 27 (1993).

[20] R. Ellis, Macromolecular crowding: Obvious but underappreciated, Trends Biochem. Sci. **26**, 597 (2001).

[21] R. J. Ellis and A. P. Minton, Join the crowd, Nature (London) **425**, 27 (2003).

[22] D. Hall and A. P. Minton, Macromolecular crowding : Qualitative and semiquantitative successes, quantitative challenges, Biochim. Biophys. Acta **1649**, 127 (2003).

[23] G. Rivas and A. P. Minton, Macromolecular crowding in vitro, in vivo, and in between, Trends Biochem. Sci. **41**, 970 (2016).

[24] M. Delarue, G. Brittingham, S. Pfeffer, I. Surovtsev, S. Pinglay, K. Kennedy, M. Schaffer, J. Gutierrez, D. Sang, G. Poterewicz, J. Chung, J. Plitzko, J. Groves, C. Jacobs-Wagner, B. Engel, and L. Holt, mTORC1 controls phase separation and the biophysical properties of the cytoplasm by tuning crowding, Cell **174**, 338 (2018).

[25] A. A. M. André and E. Spruijt, Liquid–liquid phase separation in crowded environments, Int. J. Mol. Sci. **21**, 5908 (2020).

[26] E. Spruijt, Open questions on liquid–liquid phase separation, Commun. Chem. **6**, 23 (2023).

[27] C. Alfano, Y. Fichou, K. Huber, M. Weiss, E. Spruijt, S. Ebbinghaus, G. De Luca, M. A. Morando, V. Vetri, P. A. Temussi, and A. Pastore, Molecular crowding: The history and development of a scientific paradigm, Chem. Rev. **124**, 3186 (2024).

[28] R. Berthin, J. D. Fries, M. Jardat, V. Dahirel, and P. Illien, Microscopic and stochastic simulations of chemically active droplets, Phys. Rev. E **111**, L023403 (2025).

[29] J. Fries, J. Diaz, M. Jardat, I. Pagonabarraga, P. Illien, and V. Dahirel, Active droplets controlled by enzymatic reactions, J. Roy. Soc. Interface. **22**, 20240803 (2025).

[30] M. P. Allen and D. J. Tildesley, *Computer Simulation of Liquids* (Oxford University Press, Oxford, 1987).

[31] A. P. Thompson, H. M. Aktulga, R. Berger, D. S. Bolintineanu, W. M. Brown, P. S. Crozier, P. J. in 't Veld, A. Kohlmeyer, S. G. Moore, T. D. Nguyen, R. Shan, M. J. Stevens, J. Tranchida, C. Trott, and S. J. Plimpton, LAMMPS - a flexible simulation tool for particle-based materials modeling at the atomic, meso, and continuum scales, Comput. Phys. Commun. **271**, 108171 (2022).

[32] J. D. Weeks, D. Chandler, and H. C. Andersen, Role of repulsive forces in determining the equilibrium structure of simple liquids, J. Chem. Phys. **54**, 5237 (1971).

[33] F. Oosawa and S. Asakura, Surface tension of high-polymer solutions, J. Chem. Phys. **22**, 1255 (1954).

[34] S. Asakura and F. Oosawa, Interaction between particles suspended in solutions of macromolecules, J. Polym. Sci. **33**, 183 (1958).

[35] R. Tuinier, J. Rieger, and C. De Kruif, Depletion-induced phase separation in colloid–polymer mixtures, Adv. Colloid Interface Sci. **103**, 1 (2003).

[36] K. Binder, P. Virnau, and A. Statt, Perspective: The Asakura Oosawa model: A colloid prototype for bulk and interfacial phase behavior, J. Chem. Phys. **141**, 140901 (2014).

[37] H. N. Lekkerkerker, R. Tuinier, and M. Vis, *Colloids and the Depletion Interaction*, Lecture Notes in Physics, Vol. 1026 (Springer, Cham, 2024).

[38] I. M. Sokolov, Models of anomalous diffusion in crowded environments, Soft Matter **8**, 9043 (2012).

[39] F. Höfling and T. Franosch, Anomalous transport in the crowded world of biological cells, Rep. Prog. Phys. **76**, 046602 (2013).

[40] O. Benichou, P. Illien, G. Oshanin, A. Sarracino, and R. Voituriez, Tracer diffusion in crowded narrow channels. Topical review, J. Phys.: Condens. Matter **30**, 443001 (2018).

[41] B. J. Ackerson and L. Fleishman, Correlations for dilute hard core suspensions, J. Chem. Phys. **76**, 2675 (1982).

[42] S. Hanna, W. Hess, and R. Klein, Self-diffusion of spherical Brownian particles with hard-core interaction, Phys. A (Amsterdam) **111**, 181 (1982).

[43] H. N. W. Lekkerkerker and J. K. G. Dhont, On the calculation of the self-diffusion coefficient of interacting Brownian particles, J. Chem. Phys. **80**, 5790 (1984).

[44] D. Zwicker, O. W. Paulin, and C. ter Burg, Physics of droplet regulation in biological cells, Rep. Prog. Phys. **88**, 116601 (2025).

[45] J. D. Fries, R. Berthin, C. Luo, M. Jardat, D. Zwicker, V. Dahirel, and P. Illien, Dataset associated with "Chemically active droplets in crowded environments" [Data set], Zenodo (2025), https://doi.org/10.5281/zenodo.17642201.

[46] Y. Qiang and D. Zwicker, Flory: A Python package for finding coexisting phases in multicomponent mixtures, J. Open Source Software **10**, 7388 (2025).

[47] D. Zwicker, py-pde: A Python package for solving partial differential equations, J. Open Source Software **5**, 2158 (2020).